Research Article Vol. 13, No. 5 / 1 May 2023 / Optical Materials Express 1440
Optical Materials EXPRESS

Vacuum ultraviolet optical properties of GaSb determined by synchrotron rotating analyzer ellipsometry: applications in nanopillars and plasmonics

Nathan Hale,[1] Victoria M. Bjelland,[1,2] Christoph Cobet,[3] Norbert Esser,[4,5] and Morten Kildemo[1,*]

[1]*Department of Physics, Norwegian University of Science and Technology (NTNU), NO-7491, Norway*
[2]*European Organization for Nuclear Research (CERN), CH-1211 Geneva, Switzerland*
[3]*Linz School of Education, Johannes Kepler Universität Linz 4040 Linz, Austria*
[4]*Institut für Festkörperphysik, Technische Universität, Berlin, Hardenbergstr 36, 10623 Berlin, Germany*
[5]*Leibniz-Institut für Analytische Wissenschaften–ISAS–e.V., Schwarzschildstrasse 8, 12489 Berlin, Germany*
[*]*morten.kildemo@ntnu.no*

Abstract: The vacuum ultraviolet (VUV) optical properties in the range 4 eV to 15 eV of GaSb have been determined by rotating analyzer ellipsometry (RAE) using synchrotron light. The localized surface plasmon resonances (LSPRs) and surface plasmon polaritons (SPPs) are studied as a means to understand the plasmonic behavior of GaSb. The large imaginary part of the dielectric function causes poor confinement of the SPP. Self-assembled GaSb nanopillars of 35 nm height are studied experimentally by RAE at different angles of incidence. The pillars are simulated numerically using an effective medium approach and the finite element method (FEM), where clear similarities between the simulations and experiment are observed. Additional dips in the reflectivity accompanied by increased nanopillar absorption and local field enhancement were observed near the surface of the pillars. These results demonstrate GaSb nanopillars to be promising candidates for photocathodes.

1. Introduction

The optical properties of III-V semiconductors are well studied at infrared, visible and near-ultraviolet frequencies. This has allowed for the investigation of phonons, the Drude-like effects of doping and the main critical points in the NIR-VIS-UV range [1]. At infrared and visible frequencies, GaSb has been relevant in the study of photodiodes, low threshold voltage lasers and thermo-photo-voltaics [2].

Here, the focus is shifted to the vacuum ultraviolet (VUV), exploring synchrotron-based spectroscopic-ellipsometry (SE) measurements to both extract the dielectric function of c-GaSb and to study nanopatterned GaSb surfaces. Similar to other semiconductors [3,4], metallic properties can be observed in the VUV due to strong electronic resonances at frequencies above the bandgap. In this work, the metallic properties of GaSb are demonstrated and the plasmonic phenomena are studied. These plasmonic properties, including surface plasmon polaritons (SPPs) and localized surface plasmon resonances (LSPRs) are modeled using numerical techniques such as the finite difference time domain (FDTD) and finite element method (FEM).

The VUV optical response of semiconductors and metals have also received a renewed interest due to the appearance of deep and extreme ultraviolet lithography (DUV/EUV lithography). As an example, UV-SPPs could in principle be explored in contact lithography for sub-diffraction resolution lithography [5]. On the other hand, the lack of control of LSPRs and SPPs in contact lithography can result in unwanted surface roughness, reducing the resolution [5].

#483230 https://doi.org/10.1364/OME.483230
Journal © 2023 Received 12 Dec 2022; revised 27 Jan 2023; accepted 9 Feb 2023; published 27 Apr 2023

Optical Materials EXPRESS

GaSb has also been demonstrated to self-assemble, forming nanopillar structures through low-ion-energy bombardment [6,7]. The pillars congregate in an near-hexagonal pattern. A uniaxial Bruggeman-effective-medium-approximation (BEMA) has been shown to approximate the experimental data in the visible range [8–10]. It is important to investigate how these models extend into the VUV range, both for metrology and device purposes. An alternative is to use the FEM method to simulate the data which would better include the plasmonic properties found in GaSb.

III-V semiconductors have long been considered suitable photocathode materials [11,12]. The quality of photocathodes is directly related to the quantum efficiency (QE) of the material surface, determined by the photon-absorption of the electrons, their escape depth and their ability to overcome the escape potential [12,13]. With relation to photocathodes, previous studies have focused on the QE and photoelectron transport of GaAs [14,15] in the visible as well as wide band gap semiconductors such as GaN in the UV [12]. Here, focus is placed on nanostructured GaSb, where dips in the reflectivity in the VUV-range with corresponding peaks in the heat loss, and field enhancements are demonstrated, making it an interesting candidate as a photocathode-material [15–19].

2. Experiment

2.1. Synchrotron measurement procedure for bulk GaSb and nanostructured GaSb

The VUV-RAE was performed using the U125/2-NIM beamline at the research establishment Berlin Electron Storage Ring for Synchrotron Radiation (BESSY). The exact angle of incidence was calibrated for each loaded sample. Measurements in the range of 4.2 eV to 9.8 eV were performed using a MgF_2 polarizer at the entrance of the chamber and a rotating MgF_2 analyzer, with an angle of incidence to the sample at 67.85 ° for the bulk GaSb. The same setup was used for the nanopillar samples, but for 3.1 eV to 10.0 eV. Measurements in the range of 10 eV to 23.6 eV for the bulk GaSb were performed using a triple gold rotating analyzer, with an angle of incidence on the sample at 45.0 °. The nanopillars were measured in the range 9 eV to 25 eV with the same setup. In this range, no polarizer was used due to the linear polarization of the synchrotron radiation (> 99 %). The VUV-RAE at BESSY was a standard rotating analyzer ellipsometer [20], except that the sample and the analyzer were rotated with respect to the polarizer and the light source. This was in order to obtain the rotation of the polarizer with respect to the incidence plane.

The intensity recorded for a RAE detector is given by [21]

$$I(t) = I_0\left(1 + c_2\cos\left(2A(t)\right) + s_2\sin\left(2A(t)\right)\right), \tag{1}$$

where A(t) is the real orientation of the analyzer, while c_2 and s_2 are the derived Fourier coefficients. The corresponding intensity calculated by the Jones or Mueller matrix formalism has the form

$$I(t) = I_0\left(1 + \alpha\cos\left(2\chi(t)\right) + \beta\sin\left(2\chi(t)\right)\right), \tag{2}$$

where I_0 is proportional to the total reflectance of the sample and the ideal angle χ(t)=A(t)-A_0, where A_0 is the offset of the analyzer. The coefficients α and β relate to the measured Fourier coefficients through the following equations

$$\begin{aligned} \alpha &= \eta\left(c_2\cos\left(2A_0\right) + s_2\sin\left(2A_0\right)\right), \\ \beta &= \eta\left(-c_2\sin\left(2A_0\right) + s_2\cos\left(2A_0\right)\right), \end{aligned} \tag{3}$$

with the additional electronics parameter η. Calibration prior to the measurements involves determining the offset angle A_0, the electronics parameter η, in addition to the small mechanical offset of the polarizer with respect to the incidence plane, P_0. The calibration of these parameters

Optical Materials EXPRESS

is usually performed on each new sample entering the chamber. However, the calibration for the nano-patterned sample proved to be more difficult. This was mostly due to the low reflectivity, but possibly also due to a minor tilt of the pillars. The solutions consisted of either using the non-patterned corners of the sample, or previous calibration parameters from a flat, isotropic sample. All measurements were performed with almost the same polarizer orientation with respect to the incidence plane. This angle was typically set to $\xi = (20^\circ - P_0)$, where P_0 was found near 0°. The ellipsometric quantities tan(Ψ) and cos(Δ) are defined for an isotropic sample by [22]

$$r_p/r_s = \tan(\Psi)\exp(i\Delta), \tag{4}$$

where r_p and r_s are the Fresnel reflection coefficients. They were calculated from the measured Fourier coefficients as

$$\tan\Psi = \sqrt{\frac{1+\alpha}{1-\alpha}}\,|\tan\xi|\,, \qquad \cos\Delta = \frac{\beta}{\sqrt{1-\alpha^2}}\mathrm{sgn}(\xi). \tag{5}$$

Near-infra-red-visible-ultraviolet (NIR-VIS-UV) ellipsometric measurements of a clean (native oxidized) sample and a nanopatterned sample were performed using standard commercial spectroscopic ellipsometers (0.6 eV-6.5 eV with UVISEL Horiba Jobin Yvon, and 0.73 eV-5.9 eV using RC2, J.A. Woollam Co.).

2.2. Clean c-GaSb preparation

The bulk GaSb sample was a single-side polished purposely Te-doped, c-GaSb wafer, with an n-type doping level of $3{\cdot}10^{17}\mathrm{cm}^{-3}$, determined by Hall effect measurements. The sample was cleaned in an ultrasonic bath, dipped in HCl for 1 minute, then loaded within 5 minutes into the ultra-high-vacuum (UHV). The sample was then heated to 300° C, while monitoring the increase of the peak in Im(ϵ) at 5.2 eV. Lastly, the sample was cooled to room-temperature and measured using the VUV-RAE. This procedure is expected to remove the surface oxide, but also created some surface roughness.

2.3. Nanopillar manufacturing

The GaSb nanopillars were fabricated through a self-assembly process involving low ion-energy bombardment (Ar^+) on a clean GaSb substrate, described in detail elsewhere [6,7,23]. The Ar^+ ions were applied with an energy of 300 eV to 500 eV at a flux of 14 $\mathrm{mA/cm}^2$ for a duration of 10 minutes.

Figure 1(a) and (b) show the AFM and SEM images of samples manufactured with similar processing conditions, respectively. The pillars typically form a near hexagonal pattern of pillars. The SEM and AFM images of the nanopatterned surface show a random distribution of nanopillars, with an average number of 6 neighbors. The nanocone density was determined to be 711 ± 56 cones/μm^2 from the SEM image. A hexagonal distribution results in an effective lattice constant of $|a_1| = 40.4$ nm. The Voronoi tessellation technique applied to the SEM image resulted in an average cone separation of $\langle d\rangle = 42.2$ nm with a standard deviation of 10 nm, while a similar analysis of the AFM image resulted in $\langle d\rangle = 45$ nm. Other typical AFM and SEM images of such cones are found in Refs. [6,8,9,23,24].

2.4. Numerical modeling

The scattering of small unsupported particles was modeled using the FDTD method (using the Lumerical 2021 R1.1 software package from Ansys). Both scattering cross-sections and field profiles were recorded. The parameters of the simulations included a mesh size of 0.4 nm around the particle, a total-field scattered-field source and perfectly matched layer boundary conditions along all directions.

Optical Materials EXPRESS

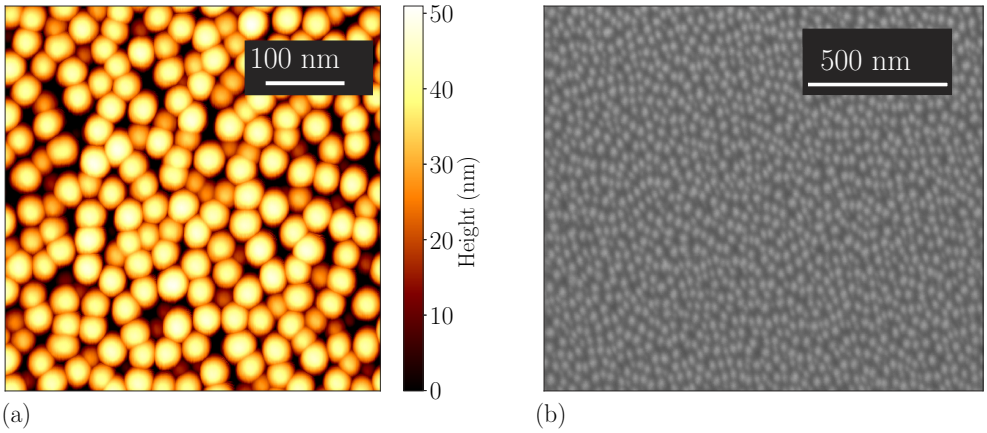

Fig. 1. (a) AFM image taken over a 500 × 500 nm range showing a 100 nm rule for scale. The color map represents the height of the cones from 0 to 50 nm. (b) SEM image of the cones with a 500 nm rule depicting the scale taken with 70k × magnification.

The simulated Jones matrix elements of the GaSb nanopillar system (GaSb nanopillars on GaSb substrate), as shown below in Fig. 5, and thus the corresponding Mueller-Jones elements were obtained using the FEM. These were extracted from the S-parameters calculated using COMSOL multiphysics 5.4, with the wave optics module, through two separate calculations for p (TM) and s (TE) polarized incidence, and where the unit cell used periodic boundary conditions and all diffracted modes were included in the calculations [25]. The minimum mesh was proportional to the wavelength and the mesh was updated for every wavelength. To account for the large variations in the refractive index of GaSb across the full spectral range, the mesh size was also scaled down by the maximum refractive index in the simulation range. The simulations across such a large spectral range was performed in three steps; 53 nm to 124 nm in steps of 1 nm with a maximum refractive index 1.0, 125 nm to 250 nm in steps of 5 nm and 255 nm to 450 nm in steps of 5 nm (the latter two with a maximum refractive index of 5.24 in mesh calculations).

3. Results and discussion

3.1. Dielectric function of c-GaSb

Figure 2 shows the complex dielectric function ϵ of c-GaSb determined from the combination of NIR-UV and VUV-RAE measurements in the range 0.7 eV to 23.0 eV. Data from Aspnes and Studna is used in the range 1.5 eV to 6 eV [26]. The data from 0.7 eV to 1.5 eV was complemented by standard PMSE measurements on the c-GaSb.

The surface roughness was modeled by a BEMA layer consisting of 50 % void and 50 % c-GaSb. The overlayer was mathematically removed, resulting in the dielectric function of bulk c-GaSb. The thickness of the surface layer was chosen such that the VUV-RAE dataset would match the Aspnes dataset [26] in the overlapping range (>3.1 eV). The measured dielectric function was extended from 6 eV to 9.8 eV and 10 eV to 23.6 eV. Due to poor signal at certain energies, the gap in photon energy is from 9.8 eV to 12 eV. To compensate for the missing data, the gap was interpolated before using the B-spline method to ensure the dielectric function remained Kramers-Kronig consistent. This procedure slightly alters the entire dataset from the measured one.

The optical properties of bulk GaSb have been previously described in literature up to 5 eV [27]. Most notably, the region is dominated by the E_0 (direct band gap), E_1, $E_1 + \Delta_1$ and E_2 resonances, being described as critical points of band-to-band transitions, including excitonic

Optical Materials EXPRESS

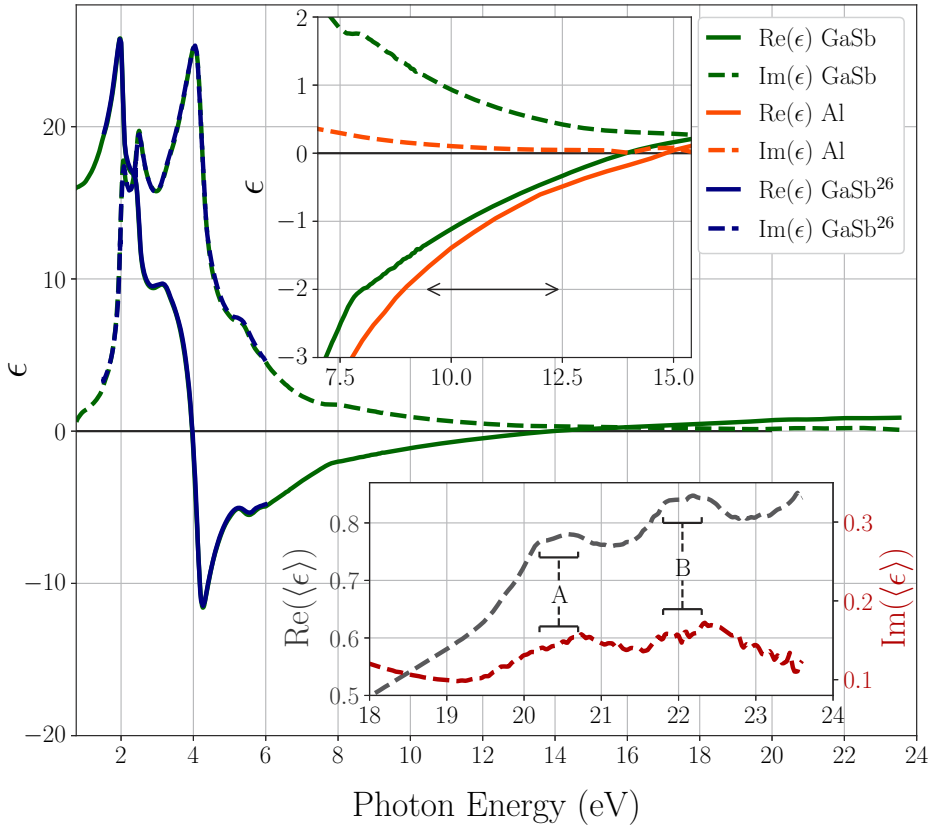

Fig. 2. The real (green lined) and imaginary (green dashed) components of the dielectric function ϵ as a function of energy for crystalline GaSb, with data from Aspnes and Studna included in the range 1.5 eV to 6 eV [26]. The top inset shows the dielectric functions of both GaSb and Al, with a focus on the plasmonic region from 7 eV to 15.5 eV. The double-headed arrow represents the interpolated region from 9.37 eV to 12.5 eV. The bottom inset is a magnification of the DUV region for the pseudo-dielectric function $\langle\epsilon\rangle$ of bulk GaSb, where the core level to the conduction band (CB) resonances A and B are visible.

effects [27]. At photon energies above these resonances, Re(ϵ) becomes negative, exhibiting metallic properties as seen in Fig. 2 from 4 eV to 14 eV. Additional possible critical point features are observed in this plasmonic region occurring at approximately 5.5 eV and 8 eV (and potentially around 15 eV). Beyond 8 eV, the response is Drude-like, as described for other semiconductors (Si, Ge, GaAs, InSb and GaP). This was explained by the valence electrons behaving essentially as unbound electrons [3]. However, new spectral features in the dielectric function are also observed in the range between 20 eV and 23 eV. These features, denoted A and B in Fig. 2 (bottom inset) have been well described in the literature for materials similar to GaSb, such as GaN and are due to transitions between non-dispersive Ga 3d core levels and the conduction band [28]. In particular, the measured pseudo-dielectric function prior to the Kramers-Kronig consistent B-spline processing, shows that the typical 0.4 eV spin orbit splitting of the Ga 3d core level results in a double peak feature around 20.5 eV and similarly around 22.2 eV [29]. The two latter features may be related to the two first peaks in the inverse photoemission spectra [30].

Optical Materials EXPRESS

3.2. Plasmonic phenomena

Plasmonics is the research of how metallic materials can enhance and confine light [31]. By comparing GaSb to a standard material, the quality and scale of these plasmonic effects can be understood. Aluminium (Al) provides a good material for comparison, having a similar dielectric function to GaSb over their plasmonic regions, as seen in Fig. 2 (top inset). The optical properties of Al were taken from Palik [32].

3.2.1. Localized surface plasmon resonance

The localized surface plasmon resonance (LSPR), also known as the Fröhlich condition, is a plasmonic phenomenon that occurs in this metallic region [33]. Assuming the surrounding medium is vacuum/air, the generalized polarizability tensor ($\bar{\alpha}$) of an elliptical particle has diagonal elements [31,33]

$$\alpha_{\mathrm{i}} = 4\pi a_1 a_2 a_3 \frac{\epsilon - 1}{3 + 3L_{\mathrm{i}}(\epsilon - 1)}, \qquad \mathrm{i} = x, y, z, \tag{6}$$

where a_1, a_2 and a_3 are the semi-axes of the ellipse, L_i is the depolarization factor (in the ith direction), and ϵ is the relative permittivity of the particle. This depolarization factor L_i describes the geometry of the particle with values $L_i = 0$, $\frac{1}{3}$ and 1 describing horizontal planes, spheres and vertical wires, respectively. For a spherical particle with no loss, this results in a divergence at Re(ϵ) = -2. For real materials however, a negative Re(ϵ) is accompanied by a non-zero Im(ϵ) component and the resonance is accordingly broadened and red-shifted. This is seen in Fig. 3, where the scattering cross-sections and electric field profiles for spherical particles of radius 15 nm have been simulated using FDTD for both GaSb and Al. Figure 3(a) shows that the resonance peak for GaSb is weaker and at a slightly higher energy of 7.75 eV compared to that of Al, which has a resonance at 7.2 eV. This weaker, broader resonance for GaSb is consistent with the larger Im(ϵ) component seen in Fig. 2 (top inset). Figures 3(b) and (c) show the absolute value of the y component of the electric field over a cross-section of a particle of Al and GaSb, respectively. Both sub-figures show a dipole-like resonance, which is expected as the incoming light was linearly polarized along the y direction. However, the field strength is approximately 3 times higher for the Al particle. Both the scattering cross-section and field profiles show the resonance is more suppressed for GaSb.

3.2.2. Surface plasmon polariton

SPPs are coupled modes in which energy is partitioned between electrons in a medium with Re(ϵ) < 0 and the electric field in a medium with Re(ϵ) > 0. For interfaces where the dielectric medium is vacuum/air, the dispersion relation is given as [31]

$$k_x = \frac{\omega}{c}\sqrt{\frac{\epsilon}{\epsilon + 1}}, \tag{7}$$

where k_x is the in-plane component of the wave vector, ω is the angular frequency, c is the speed of light in vacuum and ϵ is the dielectric function of the metallic medium. For lossless materials, a resonance in k_x is seen when Re(ϵ) = -1. As in the case for LSPRs, real materials have loss and the SPP resonance is broadened and weakened. This is seen in Fig. 4(a), in which the real and imaginary components of the in-plane wave vectors are plotted against energy for both GaSb and Al as metallic semi-infinite layers. For GaSb, the SPP resonance has a maximum at 10.23 eV, which is consistent with previously performed electron-energy-loss-spectroscopy (EELS) experiments, which found the SPP frequency to be 10.3 eV [34]. EELS also showed the bulk plasma frequency to be 14.7 eV. The data seen in Fig. 2 however, shows a plasma frequency at 14 eV. This discrepancy could be accounted for by the electron-electron interactions that contribute

Optical Materials EXPRESS

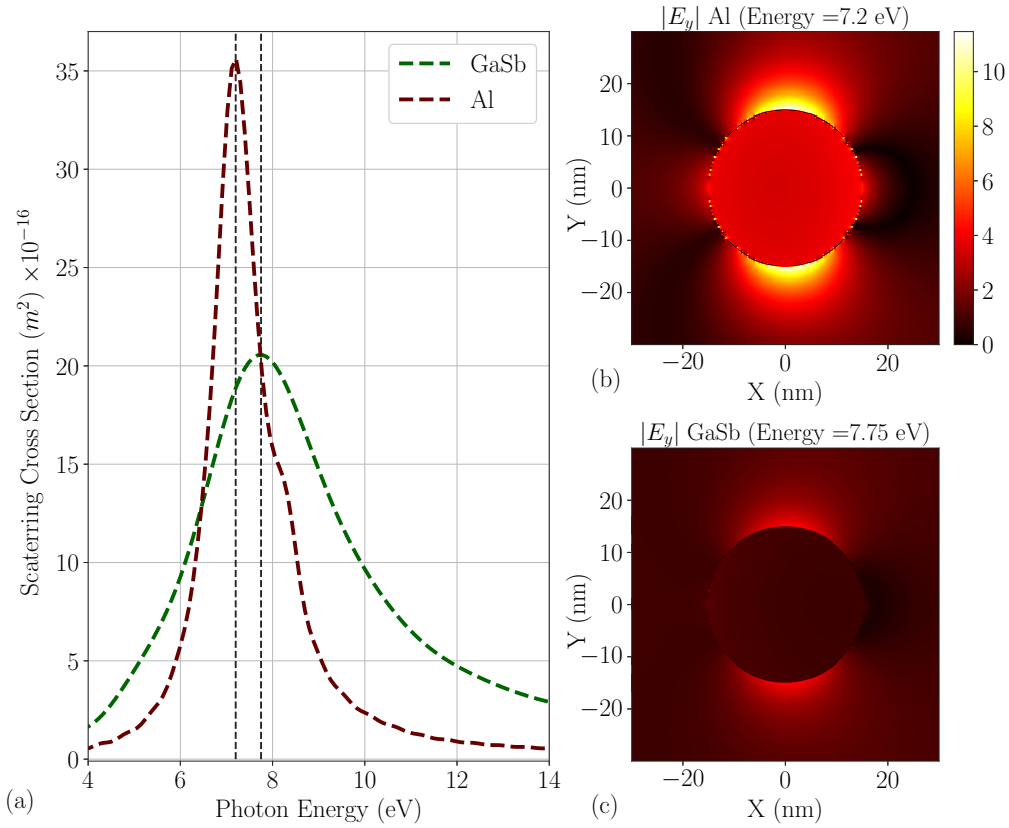

Fig. 3. (a) The scattering cross-section of a 15 nm radius particle of GaSb and Al. (b) A cross-section of the Al particle with a color-map showing the absolute values of the y component of the electric field as a function of x and y. The color-map units are dimensionless as the field has been normalized by the incident light. (c) Same as with (b), but with the GaSb particle. The energies in (b) and (c) coincide with peaks in the scattering cross-section, with Energies = 7.2 (Al) and 7.75 eV (GaSb).

to Im(ϵ) or the alterations made by the B-spline method. Other measurements place the SPP and bulk plasmon energies at 9.6 eV and 14.8 eV, respectively [35]. Figure 4(a) shows Re(k_x) is smaller for GaSb than for Al, while Im(k_x) is larger for GaSb than for Al. The smaller Re(k_x) values point towards a lower confinement factor for the SPPs with GaSb. The larger Im(k_x) indicates a shorter propagation length (the length at which the polariton has decayed by a factor of e). Figure 4(b) shows both the confinement factor and propagation length as a function of energy. The figure clearly demonstrates that Al has a higher/better confinement factor and a longer/better propagation length than GaSb, indicating that GaSb is an inferior candidate for utilizing SPPs to confine and enhance electric fields.

3.3. VUV optical response of self-assembled nanopillar array of GaSb on bulk GaSb

Returning to the GaSb nanopillar sample shown in Fig. 1, the experimental ellipsometric parameters Ψ and Δ recorded in the range 3.1 eV to 9.8 eV are shown in Fig. 5(a) and (b) at 67.85 °, respectively. The parameters are also measured in the range 9 eV to 25 eV and shown for 45.0 ° incidence in Fig. 6. The datasets show a strong peak in Ψ around 7 eV and a dip at 10 eV.

Optical Materials EXPRESS

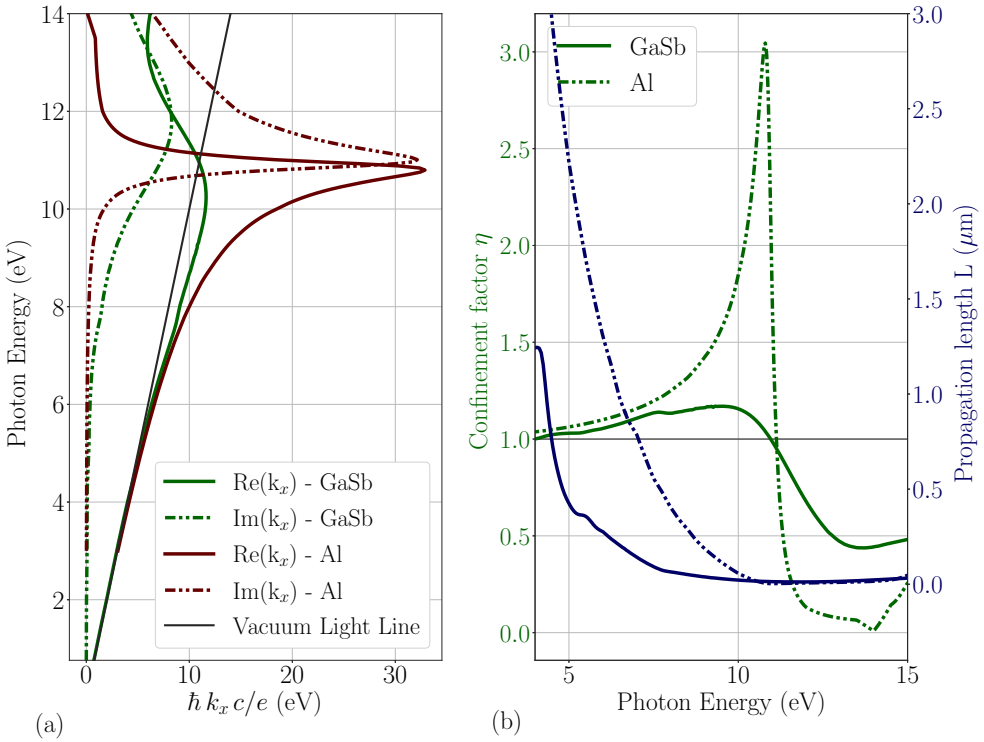

Fig. 4. (a) The dispersion relation between photon energy and in-plane wave vector (in units of eV) for both GaSb and Al, showing the real part of the in-plane wave vector (dashed line), imaginary component (dashed-dotted line) and the vacuum light line (black, dashed line). (b) The confinement factor (green) given by $\eta = \mathrm{Re}(k_x)c/\omega$ and the propagation length given by $L = 1/\mathrm{Im}(2k_x)$ (blue) as a function of photon energy. GaSb and Al are shown by the dashed and dashed-dotted lines, respectively.

3.3.1. Modeling using simplified uniaxial BEMA

In the visible range, the dielectric tensor of the effective uniaxial layer representing short pillars (height h < 100 nm) and tilted cones [10] is modeled well using a uniaxial BEMA [8] given by [9]

$$f\frac{\epsilon_{\mathrm{GaSb}}-\epsilon_{\mathrm{ii}}}{\epsilon_{\mathrm{ii}}+L_i(\epsilon_{\mathrm{GaSb}}-\epsilon_{\mathrm{ii}})}+(1-f)\frac{\epsilon_{\mathrm{void}}-\epsilon_{\mathrm{ii}}}{\epsilon_{\mathrm{ii}}+L_{\mathrm{i}}(\epsilon_{\mathrm{void}}-\epsilon_{\mathrm{ii}})}=0, \qquad \mathrm{i}=x,y,z \tag{8}$$

where f is the volume fill factor and ϵ_{GaSb}, ϵ_{void} and ϵ_{ii} are the complex dielectric functions of GaSb, vacuum and the effective medium layer representing the pillars, respectively. Meanwhile, $L_x = L_y = L_{||}$ and L_z are the in-plane and out-of-plane depolarization factors, respectively. The tensor ϵ_{ii} was oriented such that the components ϵ_{xx} and ϵ_{yy} were perpendicular to the cylinder axis, while the component ϵ_{zz} was parallel. On average the GaSb pillars have 6 nearest neighbors, hence the filling factor is calculated for a hexagonal lattice as [8]

$$f=\frac{\pi}{\sqrt{12}}(D_1)^2. \tag{9}$$

Notably, the above discussed metallic character of GaSb in the VUV is expected to have an impact on the resonant behavior of the nanopillars near the LSPR and may also lead to sharp minima in reflection, such as topological darkness points [36].

Optical Materials EXPRESS

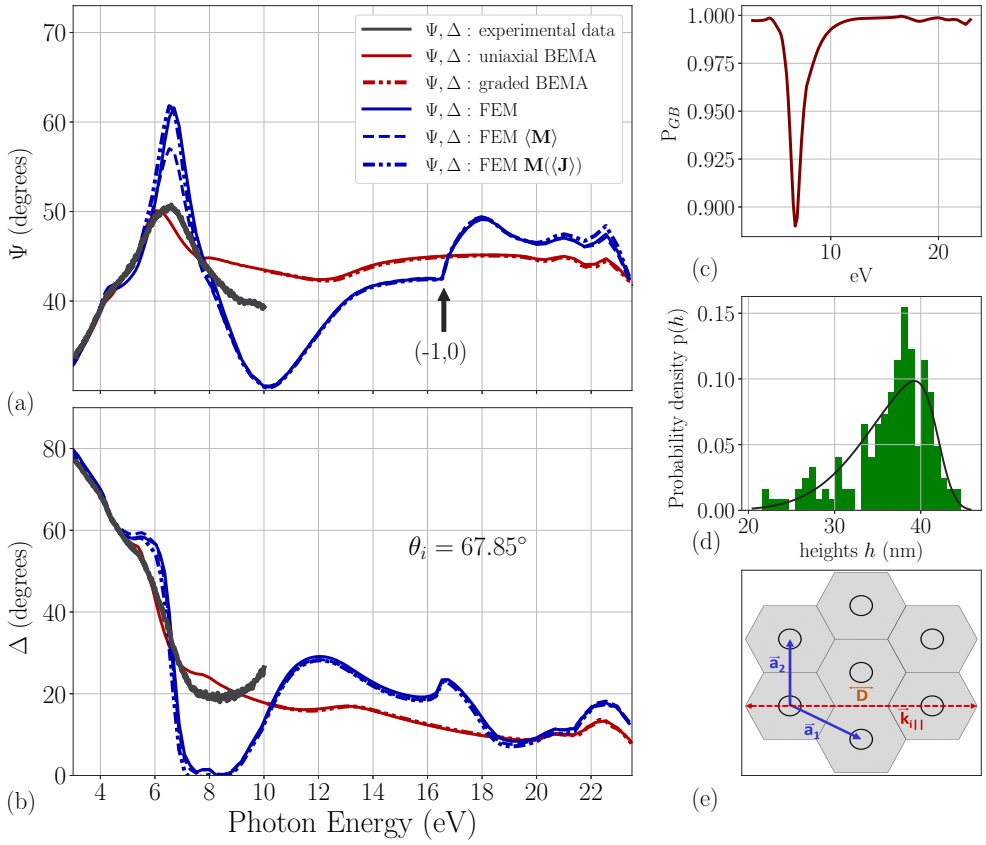

Fig. 5. Experimental and simulated ellipsometric spectra of (a) Ψ and (b) Δ of cylindrical nanopillars of GaSb on bulk GaSb. Experimental RAE data (black), the simulated BEMA model (red), the simulated BEMA model with graded pillar fill factor (red dashed-dotted), the FEM simulated data without averaging (blue), with averaging over Mueller matrices (blue dashed) and with averaging over Jones matrices (blue dashed-dotted). The onset of diffraction is labeled in (a), indicating the (-1,0) Rayleigh line (directed parallel to the plane of incidence). (c) The degree of polarization P_{GB} as a function of photon energy. (d) The fitted probability density of the distribution of pillar heights p(h). (e) The geometry of the hexagonal lattice of the cylindrical nanopillars, with $\vec{a}_1$ and $\vec{a}_2$ being the lattice parameters such that $|\vec{a}_1| = |\vec{a}_2| = d = 45$ nm, D being the cylinder diameter and $\vec{k}_{i||}$ representing the plane of incidence.

In this work, two different BEMA models were used. The simpler model consisted of one layer representing pillars with constant width and height. The more complex model consisted of 10 distinct uniaxial BEMA layers, dividing the pillar into sections of equal height. To represent the realistic features of the pillars, the fill factor of each layer was varied, such that the pillar width decreased for increasing cone height [8].

The starting point of the current analysis involved fitting the uniaxial BEMA (using CompleteEase software, J.A. Woollam Co.) to the experimental VUV-RAE data in the range 3.1 eV to 10 eV. This model is greatly simplified, as it ignores potential contributions from a-GaSb, an oxide coating and the small tilt of the pillars [8,9]. Two BEMA models were made for each measurement, where the fill factor was modeled as either constant or linearly graded. The former model (denoted uniaxial BEMA) had fitting parameters $h = 35$ nm, $L_z = 0.09$, $L_{||} = 0.455$ and f

Optical Materials EXPRESS

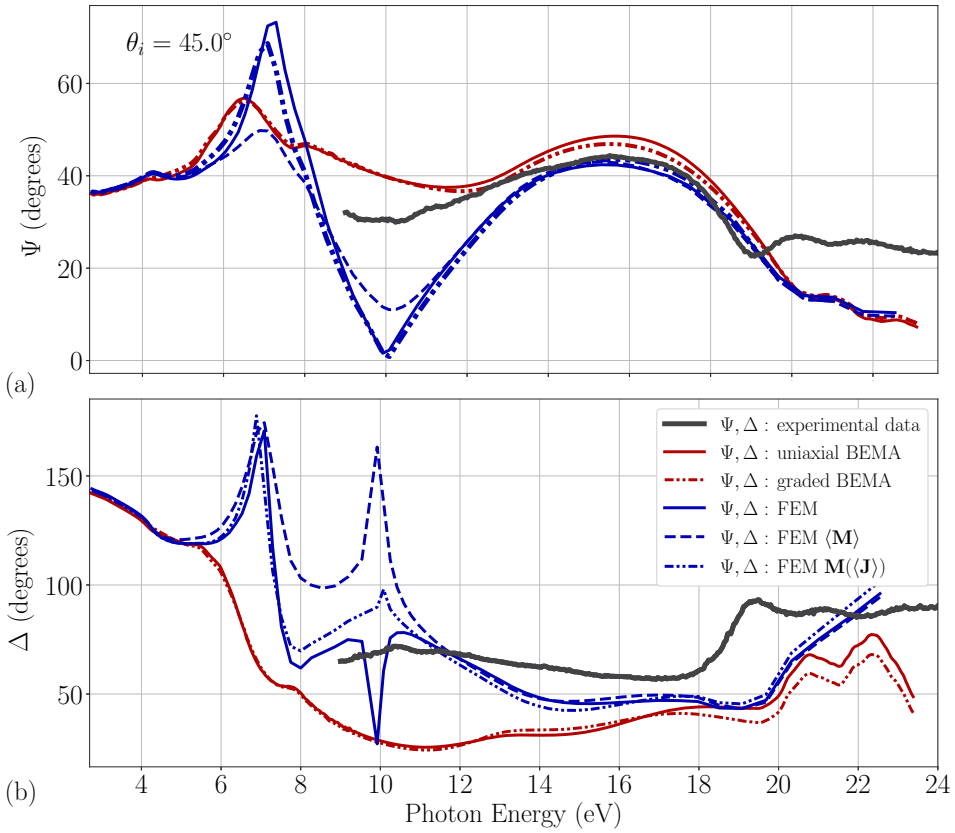

Fig. 6. Experimental and simulated ellipsometric spectra of (a) Ψ and (b) Δ of cylindrical nanopillars of GaSb on bulk GaSb. RAE data was recorded at 45.0 ° incidence in the range 9 eV to 24 eV (black), the simulated BEMA model (red), the simulated BEMA model with graded pillar fill factor (red dashed-dotted), the FEM simulated data without averaging (blue), with averaging over Mueller matrices (blue dashed) and with averaging over Jones matrices (blue dashed-dotted).

= 18.9 %. The latter model (denoted graded BEMA) had fitting parameters h = 40 nm, L_z = 0.15, $L_{||}$ = 0.425 and f = 26.6 % at the bottom and f = 11.0 % at the top of the pillars. The sensitivity to the conical shape does not appear to increase in the VUV range, see the Supplement 1.

3.3.2. Finite element method model

The simplified system of uncoated, upright pillars imposing a hexagonal pattern was used to obtain a FEM model, having d = 45 nm in accordance with the analysis of AFM patterns from Fig. 5 (d). The Jones matrix was calculated from this model, using COMSOL [25]. The spectra were calculated in the range 3.1 eV to 24 eV with the parameters extending over h = (20, 25, 30 $\cdots$ 45, 50) nm, D_1 = (0.4, 0.41,..0.49, 0.5) d and corresponding volume fill factors f = (14.5, 15.2,.., 22, 22.7) %. The minimum MSE = $(\Psi_{exp} - \Psi(D_1, h, d))^2$ in the spectral range of 3.1 eV to 5.0 eV corresponded to h = 35 nm and D_1 = 0.46 d=20.7 nm. These parameters were also used for simulating the full spectra at 67.85 ° and 45.0 ° angles of incidence. Although this is not a unique fit due to the large uncertainties around the peak and that only Ψ was fitted, it gives a consistent dataset between the BEMA and FEM simulations, shown in Figs. 5 and 6 [25]. The FEM model enables calculation of the reflectivity, heat losses (given by $\int J(r,z) \cdot E(r,z) dV$, where V is the

Optical Materials EXPRESS

volume, $E(r, z)$ is the electric field, and $J(r)$ is the current density) and corresponding field plots in and around the pillars, as seen in Fig. 7.

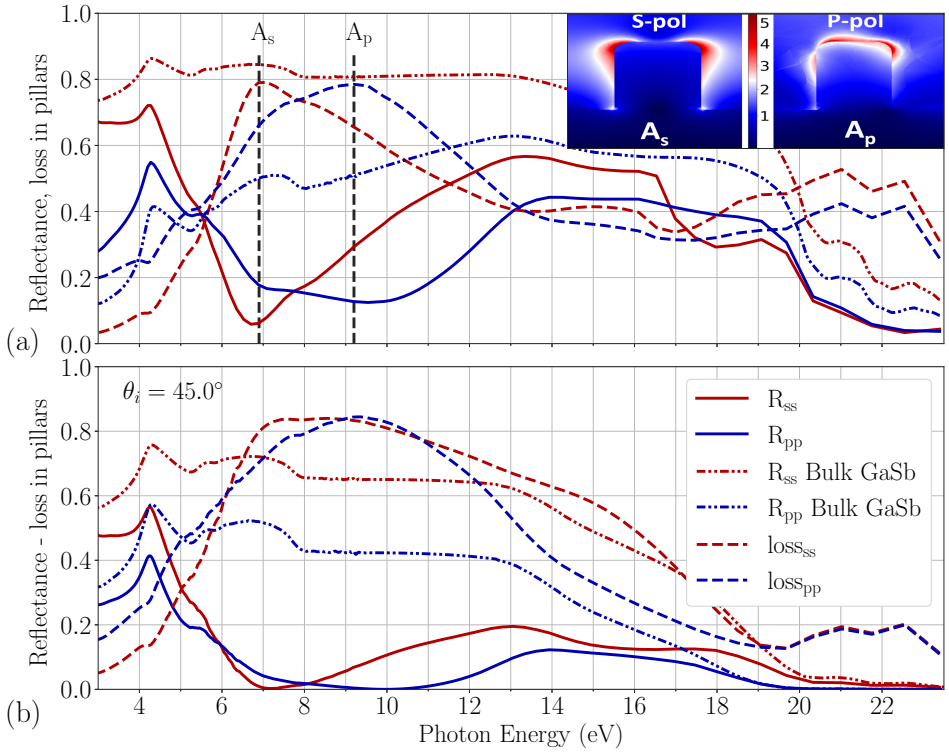

Fig. 7. The simulated reflectance and heat loss as a function of photon energy, with s-polarization (red curves) and p-polarization (blue curves). The reflectance of the GaSb nanopillars system (full lines) and the bulk GaSb (dashed-dotted lines), in addition to the heat loss (the dashed lines) are shown for polar angle of (a) $\theta_i = 67.85°$ and (b) $\theta_i = 45.0°$. The inset in (a) shows cross section plots of the absolute values of the electric field (with the color bar in units of 10^9 V/m) at the energies labelled A_s and A_p for s- and p-polarizations respectively.

Both the experimental and particularly the simulated data at 67.85 ° in Fig. 5 show a strong peak in Ψ around 7 eV, accompanied with a phase jump in Δ. The FEM model indicates that these peaks arise from a minimum in the s-reflectivity R_{ss}, as seen in Fig. 7. The loss in reflectivity coincide with the maximum in the heat-loss of the nanopillars [25], indicated by the vertical dashed line A_s in Figs. 7. The RAE data in Figs. 5 and 6 further show a dip in Ψ around 10 eV. This is better demonstrated in the FEM simulations as a dip in R_{pp} at 9.6 eV for 67.85 ° and a broader peak around 10 eV for 45.0 °, indicated by A_p in Fig. 7 accompanied by another broad peak in the heat-loss in the GaSb pillars, respectively.

The peak in Ψ is the result of the optical properties of the effective layer. Together with its strong dependence on the thickness, it is suggested that the minimum in R_{ss} is likely a type of topological darkness [36]. The FEM model further shows sharp, well defined peaks and dips appearing at 7 eV and 10 eV, and these are much more defined than for the measured data. On the other hand, the FEM model allows to identify these weaker points in the experimental data, see Fig. 5. The attenuation of the latter peaks in the experimental data, can be a result of the disorder in the morphological parameters describing the sample surface. These VUV-RAE measurements can therefore be highly useful for optical metrology.

Optical Materials EXPRESS

For s-polarization, the maximum field strength is found at A_s, as seen in the field maps in Fig. 7. This field is 3 times the field strength at point A_p. There is a strong asymmetry due to the angle of incidence being 67.85 ° for the p-polarized light. However, the maximum field strength is comparable to the maximum field strength of A_s for s-polarized light. At normal incidence, both FEM and BEMA based simulations show a broad reflectance minimum in the range 8 eV to 13 eV.

3.3.3. Effective medium model – resonances

The LSPR for s-polarized light with an in-plane depolarization factor $L_{||} = 0.5$ is expected to occur at 10.3 eV. Comparably, the LSPR for a lossless GaSb sphere occurs at 8 eV using Eq. (6). It is expected that the real resonance is red-shifted by the presence of the GaSb-substrate and by the non-zero Im(ϵ) and the finite size of the particles, as seen in Fig. 3 (a). Figure 8 shows the dielectric tensor functions for the effective layer obtained using the uniaxial BEMA and a uniaxial implementation of the Maxwell-Garnett-EMA (MGEMA) model to extract the uniaxial dielectric functions of the simulated FEM data from 67.85 °. Here, we have chosen ellipsoidal inclusions that fill uniformly a large ellipsoid of a similar shape [37]. The parameters of the MGEMA were fitted by reducing the Mean Square Error between the FEM simulated Ψ, Δ data and the MGEMA based simulated data. The nanopillar height $h = 35$ nm was fixed, while the remaining parameters were fitted giving $f = 15.7$ %, $L_z = 0.017$ and $L_x = L_y = 0.34$. Even though the interpretation of the morphological parameters is partially lost [38], this trick allows to extract a reasonable dielectric function from the FEM data.

As seen in Fig. 8, the BEMA results in broader and weaker resonances in the dielectric function than the MGEMA. The broader resonance of the BEMA smooths out the ellipsometric parameters for frequencies at which the dielectric function of GaSb has plasmonic features. The in-plane LSPR of the effective dielectric function extracted from the MGEMA shows a sharp resonance corresponding to the dip near 8.5 eV. This must correspond to the heat loss maxima around A_p in Fig. 7. Note that the peak is red-shifted from the original LSPR for a cylinder at 10.3 eV. This resonance is thus a clear signature of the plasmonic behavior of GaSb nanoparticles (and other metallic like semiconductors in this spectral range).

The simulated ellipsometric parameters based on the BEMA model were found to match the experimental VUV-RAE data reasonably well. Moreover, the morphological parameters in the BEMA model were in reasonable correspondence to microscopic imaging techniques. These findings indicate that the simple BEMA model can be used as a quick method of analysis for these types of self-assembled nanopatterned samples even at VUV energies. Previous observations [8,24] at UV-VIS wavelengths suggested a breakdown of the BEMA for shorter wavelengths (valid for $h \cdot n/\lambda < 1$). The validity of the BEMA is proposed to extend to smaller wavelengths due to the lower refractive index at these VUV photon energies.

3.3.4. Dip in reflectance and photocathode emission

Previous works have demonstrated how textured Al-based surfaces can yield excellent photoemission efficiencies at both NIR and UV wavelengths [16,39,40]. Despite having greater losses, the plasmonic features of GaSb nanostructures may also be favorable for high photoemission efficiency [15,19]. However, comparisons to both GaAs [12,15,19] and GaN [12] could be more insightful, as both semiconductors have been demonstrated to exhibit photoemission properties in the visible and UV, respectively. The photoemission, as outlined by Spicer's Three Step Model, is determined by the probability of absorption, the likelihood of electrons reaching the surface without collision and the ability of the electrons to surpass the work function [13]. Since the nanopillars experience a distinct reduction in the reflectivity, the absorption is highly increased, and the calculated loss is found to be predominantly inside and near the surface of the pillars.

Optical Materials EXPRESS

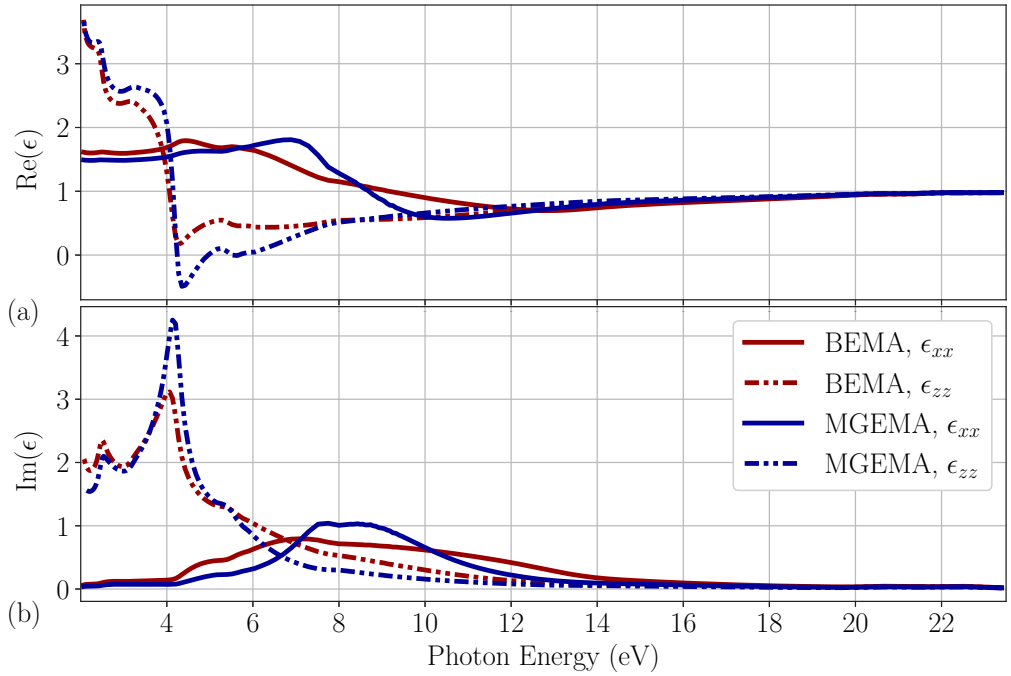

Fig. 8. The real (a) and imaginary (b) components of the uniaxial effective dielectric function of the nanopillar layer. The in-plane component ϵ_{xx} (red full lines) and out-of-plane component ϵ_{zz} (red dashed-dotted lines) are from the uniaxial BEMA fitted to the experimental data. Similarly, the in-plane component ϵ_{xx} (blue full lines) and out-of-plane component ϵ_{zz} (blue dashed-dotted line) represent the generalized uniaxial MGEMA model when fitted to the simulated FEM model data.

It has been proposed that a high near-surface absorption will reduce the electron escape path and therefore also increase the probability for the electrons to escape without recombination [16]. In addition, the field enhancement on the surface of the pillars can further improve the QE [41]. Moreover, coating the nanopatterned surface with a negative electron affinity material would allow for easy extraction [42]. Finally, the low reflectivity of the sample at these wavelengths, can help limit unwanted electron generation at the edge of the sample. Such electrons can contribute to damage inside the vacuum chamber and the cathode material itself [15].

The photoelectron transport properties [14,43] of nanostructured GaSb have not, to our knowledge, been investigated. However, n- and p- doped GaSb is reported to exhibit a strong surface space charge layer (SSCL) [44]. Combined with the large surface area of the GaSb pillars, the SSCL may extend through most of the pillars [45]. For p-type doped GaSb, the reported two SSCLs [44] appear to be a more favorable configuration for a future photo-cathode-emission experiment, as opposed to n-type doped GaSb. An advantage of self-assembled nanopatterned pillars is the limited exposure to air during manufacturing, as both low energy ion-bombardment and activation by e.g. Cs-O can be conducted in-situ. On the other hand, semiconductor cathodes suffer from reliability issues over many emission cycles [12,46]. In particular for GaSb, the heat deposited in the pillars during the transport process may be sufficient to cause Ga-segregation at the surface [6].

Finally, as GaAs has comparable plasmonic properties to GaSb [3], it is envisaged that nanopatterning GaAs surfaces can also enhance QE in the VUV through a similar argument.

Optical Materials EXPRESS

3.3.5. Averaging Mueller or Jones matrices from the FEM model

The sample has a broad distribution of heights which is quantified by estimating the distribution from the AFM data, as seen in Fig. 5(d). The fill factor depends on the distance between the pillars and also the height of them. It is suspected that the attenuation of Ψ is a result of the distribution of the morphology parameters such as height, lattice constant and diameter used to describe the effective layer. To test the effective distribution in fill factor and height, averaged Mueller matrix elements and Jones matrix elements are generated as [47]

$$\begin{aligned} \langle M\rangle_{\mathrm{ij}} &= \int M_{\mathrm{ij}}(h,f)\mathrm{p}(h)\mathrm{p}(f)\mathrm{d}h\mathrm{d}f, \qquad \mathrm{i}=1..4, \quad \mathrm{j}=1..4, \\ \langle J\rangle_{\mathrm{pq}} &= \int J_{\mathrm{pq}}(h,f)\mathrm{p}(h)\mathrm{p}(f)\mathrm{d}h\mathrm{d}f, \quad \mathrm{p}=1,2, \quad \mathrm{q}=1,2, \end{aligned} \tag{10}$$

where it is assumed an uncorrelated height and fill factor p(h)p(f), and p(f) to be a simple top hat function from 14.5 % to 22.7 %. The Mueller-Jones matrix corresponding to the averaged Jones matrix (**J**), is given by $\mathbf{M} = \mathbf{A}(\mathbf{J}\otimes\mathbf{J}^{*})\mathbf{A}^{-1}$ [48], where ⊗ is the Kronecker product and the square matrix **A** is given in the literature [48].

The results shown in Figs. 5 and 6 indicate that averaging the Jones matrices have little effect on the final result. However, averaging the Mueller matrices attenuate the Ψ peak as desired. Although the Mueller matrix averaging approach is promising, it introduces depolarization. The simple, but powerful RAE system used in the current paper without an additional retarder, cannot measure the depolarization of isotropic samples. However, measurements on a similar sample with a commercial phase modulated spectroscopic ellipsometer (PMSE) showed only a minor depolarization of 0.98 at 6.5 eV. Furthermore, the synchrotron beam is expected to have both high spatial and temporal coherence, such that there may be no measurable real depolarization at all. More complex modeling is needed for the disordered system presented here. On the other hand, the BEMA approach clearly attenuates the peak (even if we fit parameters to simulated data) without causing depolarization of the light. Indeed, the statistical foundation of the BEMA [49] may make it quite good at modeling a system with a considerable randomness in the morphological parameters.

3.3.6. Shift of Ga3d core level to CB transitions

An interesting observation in Fig. 6, is the considerable shift in the features seen in the experimental data from the nanopillars, in the range 18 eV to 24 eV, compared to the simulated data obtained using the measured bulk dielectric function. The Ga3d core level to the conduction band (CB) density of state (DOS) transition appears shifted approximately 1 eV to lower energies. This indicates that the effective nanopillar dielectric function at high energies is different from the clean bulk c-GaSb. A change in the crystallinity of c-GaSb can lead to a modification of the CB DOS states, while a lower oxidation state results in raising of the Ga3d core level, resulting in less surface oxide. More experimental work comparing the VUV-RAE with core level spectroscopy and inverse photoemission spectroscopy is needed to verify this property.

4. Conclusion

This work presents novel spectroscopic ellipsometry data on the semiconductor GaSb, showing a plasmonic region in the VUV spectral range. With comparison to Al, the LSPR and SPP resonances are shown to be broader and weaker for GaSb. The plasmonic properties are demonstrated to affect the optical response of nanopatterned GaSb. The uniaxial BEMA and the gradient uniaxial BEMA are good representations for the effective nanopillar layer, both for the low energy part of the spectrum (<6.5 eV) and the high energy part of the spectrum (>12 eV). The VUV-RAE of nanostructured GaSb demonstrates an enhanced sensitivity to

Optical Materials EXPRESS

the structured surface layer due to a dip in the reflectivity of s-polarized light followed by a dip in p-polarized light. These features are associated with strong relative phase changes between s- and p-polarized light and can be classified as topological darkness points. The FEM model better demonstrates the character of these points for ordered materials, while the RAE measurements of such self-assembled GaSb nanopillars show much weaker features, thus indicating a high sensitivity to the disorder. The low reflectivity, enhanced absorption and surface enhancement of the electric field, potentially make the GaSb pillars interesting candidates for photocathode-emission. Future RAE measurements including a fixed retarder and possibility of using the same angle of incidence for the high and low energy part of the spectrum, will allow for the measurement of depolarization and simplify data-analysis.

Funding. NTNU Nano Impact Fund; Bundesministerium für Bildung und Forschung; The Governing Mayor of Berlin-Senate Chancellery Higher Education and Research; Ministry for Culture and Science NRW; European Regional Development Fund (EFRE 1.8/07).

Acknowledgments. I.S. Nerbø and S. Leroy are acknowledged for participation in the BESSY measurements of the clean GaSb. The nanopillar sample was manufactured by S. Leroy. M. Foldyna is acknowledged for useful discussions.

Disclosures. The authors declare no conflict of interests.

Data availability. The data underlying the results presented in this paper are not publicly available at this time but may be obtained from the authors upon reasonable request.

Supplemental document. See Supplement 1 for supporting content.

References

1. S. Zollner, P. P. Paradis, F. Abadizaman, and N. S. Samarasingha, "Drude and Kukharskii mobility of doped semiconductors extracted from Fourier-transform infrared ellipsometry spectra," J. Vac. Sci. Technol., B: Nanotechnol. Microelectron.: Mater., Process., Meas., Phenom. **37**(1), 012904 (2019).
2. P. S. Dutta, H. L. Bhat, and V. Kumar, "The physics and technology of gallium antimonide: An emerging optoelectronic material," J. Appl. Phys. **81**(9), 5821–5870 (1997).
3. H. R. Philipp and H. Ehrenreich, "Optical properties of semiconductors," Phys. Rev. **129**(4), 1550–1560 (1963).
4. P. Shekhar, S. Pendharker, H. Sahasrabudhe, D. Vick, M. Malac, R. Rahman, and Z. Jacob, "Extreme ultraviolet plasmonics and Cherenkov radiation in silicon," Optica **5**(12), 1590–1596 (2018).
5. Z. Cui, *Nanofabrication - Principles, Capabilities and Limits* (Springer Cham, 2017).
6. S. Le Roy, E. Søndergård, I. S. Nerbø, M. Kildemo, and M. Plapp, "Diffuse-interface model for nanopatterning induced by self-sustained ion-etch masking," Phys. Rev. B **81**(16), 161401 (2010).
7. F. C. Motta, P. D. Shipman, and R. M. Bradley, "Theory of nanoscale pattern formation produced by oblique-incidence ion bombardment of binary compounds," Phys. Rev. B **90**(8), 085428 (2014).
8. I. S. Nerbø, M. Kildemo, S. L. Roy, I. Simonsen, E. Søndergård, L. Holt, and J. C. Walmsley, "Characterization of nanostructured GaSb: comparison between large-area optical and local direct microscopic techniques," Appl. Opt. **47**(28), 5130–5139 (2008).
9. I. Nerbø, S. Le Roy, M. Kildemo, and E. Sondergard, "Real-time in situ spectroscopic ellipsometry of GaSb nanostructures during sputtering," Appl. Phys. Lett. **94**(21), 213105 (2009).
10. I. Nerbø, S. Le Roy, M. Foldyna, M. Kildemo, and E. Søndergård, "Characterization of inclined GaSb nanopillars by Mueller matrix ellipsometry," J. Appl. Phys. **108**(1), 014307 (2010).
11. R. Bell and W. Spicer, "3-5 compound photocathodes: A new family of photoemitters with greatly improved performance," Proc. IEEE **58**(11), 1788–1802 (1970).
12. X. Wang, M. Wang, Y. Liao, L. Yang, Q. Ban, X. Zhang, Z. Wang, and S. Zhang, "Negative electron affinity of the GaN photocathode: a review on the basic theory, structure design, fabrication, and performance characterization," J. Mater. Chem. C **9**(38), 13013–13040 (2021).
13. W. E. Spicer and A. Herrera-Gomez, "Modern theory and applications of photocathodes," in *Photodetectors and Power Meters*, vol. 2022 K. J. Kaufmann, ed., International Society for Optics and Photonics (SPIE, 1993), pp. 18–35.
14. R. Zhou, H. Jani, Y. Zhang, Y. Qian, and L. Duan, "Photoelectron transportation dynamics in GaAs photocathodes," J. Appl. Phys. **130**(11), 113101 (2021).
15. X. Peng, Z. Wang, Y. Liu, D. Manos, M. Poelker, M. Stutzman, B. Tang, S. Zhang, and J. Zou, "Optical-resonance-enhanced photoemission from nanostructured Ga As photocathodes," Phys. Rev. Appl. **12**(6), 064002 (2019).
16. A. Polyakov, C. Senft, K. F. Thompson, J. Feng, S. Cabrini, P. J. Schuck, H. A. Padmore, S. J. Peppernick, and W. P. Hess, "Plasmon-Enhanced Photocathode for high brightness and high repetition rate X-Ray sources," Phys. Rev. Lett. **110**(7), 076802 (2013).
17. K. Aulenbacher, J. Schuler, D. v. Harrach, E. Reichert, J. Röthgen, A. Subashev, V. Tioukine, and Y. Yashin, "Pulse response of thin III/V semiconductor photocathodes," J. Appl. Phys. **92**(12), 7536–7543 (2002).

Optical Materials EXPRESS

18. S. Karkare, L. Boulet, L. Cultrera, B. Dunham, X. Liu, W. Schaff, and I. Bazarov, "Ultrabright and ultrafast III-V semiconductor photocathodes," Phys. Rev. Lett. **112**(9), 097601 (2014).
19. X. Peng, M. Poelker, M. Stutzman, B. Tang, S. Zhang, and J. Zou, "Mie-type GaAs nanopillar array resonators for negative electron affinity photocathodes," Opt. Express **28**(2), 860–874 (2020).
20. C. Cobet, R. Goldhahn, W. Richter, and N. Esser, "Identification of van Hove singularities in the GaN dielectric function: a comparison of the cubic and hexagonal phase," phys. stat. sol. (b) **246**(7), 1440–1449 (2009).
21. D. E. Aspnes and A. A. Studna, "High precision scanning ellipsometer," Appl. Opt. **14**(1), 220–228 (1975).
22. R. Azzam and N. Bashara, *Ellipsometry and polarized light* (North-Holland Publishing Co, 1977).
23. I. S. Nerbø, S. L. Roy, M. Foldyna, E. Søndergård, and M. Kildemo, "Real-time in situ Mueller matrix ellipsometry of GaSb nanopillars: observation of anisotropic local alignment," Opt. Express **19**(13), 12551–12561 (2011).
24. M. Kildemo, I. Nerbø, S. Hagen, S. Leroy, and E. Søndergård, "Spectroscopic ellipsometry of nanostructured GaSb surfaces consisting of densely packed 80–230nm long cones," Mater. Sci. Eng., B **165**(3), 217–220 (2009).
25. P. M. Walmsness, T. Brakstad, B. B. Svendsen, J.-P. Banon, J. C. Walmsley, and M. Kildemo, "Optical response of rectangular array of elliptical plasmonic particles on glass revealed by Mueller matrix ellipsometry and finite element modeling," J. Opt. Soc. Am. B **36**(7), E78–E87 (2019).
26. D. E. Aspnes and A. A. Studna, "Dielectric functions and optical parameters of Si, Ge, GaP, GaAs, GaSb, InP, InAs, and InSb from 1.5 to 6.0 ev," Phys. Rev. B **27**(2), 985–1009 (1983).
27. M. Munoz, K. Wei, F. H. Pollak, J. L. Freeouf, and G. W. Charache, "Spectral ellipsometry of GaSb: Experiment and modeling," Phys. Rev. B **60**(11), 8105–8110 (1999).
28. M. Rakel, C. Cobet, N. Esser, F. Fuchs, F. Bechstedt, R. Goldhahn, W. G. Schmidt, and W. Schaff, "Gan and inn conduction-band states studied by ellipsometry," Phys. Rev. B **77**(11), 115120 (2008).
29. J. Olde, K.-M. Behrens, H.-P. Barnscheidt, R. Manzke, M. Skibowski, J. Henk, and W. Schattke, "Electronic structure of the GaSb(001) surface," Phys. Rev. B **44**(12), 6312–6328 (1991).
30. A. M. Bradshaw, R. Hemmen, D. E. Ricken, and T. Schedel-Niedrig, *GaP, GaAs, GaSb, InP, InAs, InSb; Figs. 321 - 343, Tables 36 - 37: Datasheet from Landolt-Börnstein - Group III Condensed Matter · Volume 24D: "Interaction of Radiation with Surfaces and Electron Tunneling"* (Springer-Verlag Berlin Heidelberg, 1996).
31. S. A. Maier, *Plasmonics: Fundamentals and applications* (Springer, Centre for Photonics & Photonic Materials, Department of Physics, University of Bath, 2007).
32. E. D. Palik, *Handbook of Optical Constants of Solids* (Academic Press, 1985).
33. C. F. Bohren and D. R. Huffman, *Absorption and scattering of light by small particles* (John Wiley & Sons, 2008).
34. C. Raisin, F. W. O. Da Silva, and L. Lassabatere, "Oxidation study by auger electron spectroscopy and electron energy-loss spectroscopy of GaSb(001) surfaces grown by molecular-beam epitaxy," J. Vac. Sci. Technol., B: Microelectron. Process. Phenom. **8**(1), 68–74 (1990).
35. D. Mao, A. Kahn, and L. Soonckindt, "Chemical and electronic properties of the Ag/GaSb(110) interface formed at room and low temperature," Phys. Rev. B **40**(8), 5579–5587 (1989).
36. L. Malassis, P. Massé, M. Tréguer-Delapierre, S. Mornet, P. Weisbecker, P. Barois, C. R. Simovski, V. G. Kravets, and A. N. Grigorenko, "Topological darkness in self-assembled plasmonic metamaterials," Adv. Mater. **26**(2), 324–330 (2014).
37. V. A. Markel, "Introduction to the Maxwell Garnett approximation: tutorial," J. Opt. Soc. Am. A **33**(7), 1244–1256 (2016).
38. H. Wormeester, E. S. Kooij, and B. Poelsema, "Effective dielectric response of nanostructured layers," phys. stat. sol. (a) **205**(4), 756–763 (2008).
39. J. G. Endriz and W. E. Spicer, "Study of aluminum films. i. optical studies of reflectance drops and surface oscillations on controlled-roughness films," Phys. Rev. B **4**(12), 4144–4159 (1971).
40. J. G. Endriz and W. E. Spicer, "Study of aluminum films. ii. photoemission studies of surface-plasmon oscillations on controlled-roughness films," Phys. Rev. B **4**(12), 4159–4184 (1971).
41. Y. Zhou and P. Zhang, "Theory of laser-induced photoemission from a metal surface with nanoscale dielectric coating," J. Appl. Phys. **131**(6), 064903 (2022).
42. M. Kashima, Y. Itokawa, T. Kanai, D. Sato, A. Koizumi, H. Iijima, T. Nishitani, Y. Honda, H. Amano, and T. Meguro, "The photoemission characteristics of a nea InGaN photocathode by simultaneously supplying cs and o2," Appl. Surf. Sci. **599**, 153882 (2022).
43. R. Zhou, H. Jani, Y. Zhang, Y. Qian, and L. Duan, "Dynamic photoelectron transport in stepwise-doped GaAs photocathodes," Nature **12**(1), 12936 (2022).
44. J. Maslar, W. Hurst, and C. A. Wang, "Raman spectroscopy of n-type and p-type GaSb with multiple excitation wavelengths," Appl. Spectrosc. **61**(10), 1093–1102 (2007).
45. M. Kildemo, Y. I. Levinsen, S. Le Roy, and E. Søndergård, "Staircase and saw-tooth field emission steps from nanopatterned n-type GaSb surfaces," J. Vac. Sci. Technol., A **27**(5), L18–L23 (2009).
46. N. Chanlek, J. D. Herbert, R. M. Jones, L. B. Jones, K. J. Middleman, and B. L. Militsyn, "The degradation of quantum efficiency in negative electron affinity GaAs photocathodes under gas exposure," J. Phys. D: Appl. Phys. **47**(5), 055110 (2014).
47. R. Ossikovski and K. Hingerl, "General formalism for partial spatial coherence in reflection Mueller matrix polarimetry," Opt. Lett. **41**(17), 4044–4047 (2016).

Optical Materials EXPRESS

48. P. S. Hauge, R. H. Muller, and C. G. Smith, "Conventions and formulas for using the Mueller-Stokes calculus in ellipsometry," Surf. Sci. **96**(1-3), 81–107 (1980).
49. G. A. Niklasson, C. G. Granqvist, and O. Hunderi, "Effective medium models for the optical properties of inhomogeneous materials," Appl. Opt. **20**(1), 26–30 (1981).